Phase locking and multistability in the topological Kuramoto model on cell complexes

Iva Bačić *,[1,2] Michael T. Schaub ,[3] Jürgen Kurths ,[4] and Dirk Witthaut *[1,5]

[1] *Institute of Climate and Energy Systems: Energy Systems Engineering (ICE-1), Forschungszentrum Jülich, 52428 Jülich, Germany*
[2] *Institute of Physics Belgrade, University of Belgrade, Serbia*
[3] *RWTH Aachen University, Aachen, Germany*
[4] *Potsdam Institute for Climate Impact Research (PIK), Potsdam, Germany*
[5] *Institute for Theoretical Physics, University of Cologne, 50937 Köln, Germany*

Higher-order group interactions fundamentally shape the dynamics and stability of oscillator networks. The topological Kuramoto model captures these effects by extending classical synchronization models to include interactions between cells of arbitrary dimension within simplicial and cell complexes. In this article, we present the topological nonlinear Kirchhoff conditions algorithm, a nonlinear generalization of Kirchhoff's circuit laws, that systematically identifies all phase-locked states in the topological Kuramoto model and reveals how higher-order topology governs multistability. Applying this framework to rings, Platonic solids, and simplexes, we uncover structural cascades of multistability inherited across dimensions, and demonstrate that cell complexes can exhibit richer multistability patterns than simplicial complexes of equal dimension. We find evidence hinting at universal multistability classes determined by the number of boundary cells. These results reveal how higher-order interactions affect synchronization and open new directions for understanding collective dynamics in systems with non-pairwise interactions.

I. INTRODUCTION

Synchronization phenomena are a hallmark of many natural and engineered systems, from neuronal activity to power grid operation [1, 2]. The Kuramoto model of coupled oscillators has long served as a prototype for understanding how synchronization emerges from local interactions [3, 4]. While early studies focused on globally coupled systems [5], later extensions to complex networks revealed that network topology crucially shapes both the onset and the nature of synchronization [6]. Such systems often exhibit multistability, where multiple distinct synchronized states coexist [7–10].

In the classical Kuramoto model, the coupling between the oscillators is pairwise. This assumption is valid for many systems, but in certain contexts where group interactions play an essential role, such as neuronal assemblies [11], the brain connectome [12–14], multimode lasers, [15], or protein interaction networks [16], it is too restrictive to capture all the relevant couplings in the system. Higher-order connectivity structures that encode such interactions are increasingly recognized as being crucial to many collective dynamics [17–25]. Recent advances in network science [12–14, 18, 19, 23, 26–33] have introduced models where the dynamics is not defined only on nodes, but also lives on edges, faces, or higher-dimensional elements of simplicial or cell complexes. Among these, the topological Kuramoto model [34–36] has become a paradigmatic framework, revealing universal features absent in conventional networks, such as abrupt synchronization transitions [37, 38]. Moreover, topologically-induced synchronization obstructions have been found in the study of the simplicial Stuart-Landau model, where global topological synchronization has been studied [39]. While some aspects of multistability [40, 41] and phase locking [36] in similar simplicial models have been analyzed separately, there is still no systematic framework for analyzing how multistable phase-locked states emerge from higher-order interactions.

We address this gap by studying phase locking and multistability in the topological Kuramoto model defined on general cell complexes. Unlike earlier work based on the master stability function formalism [39, 42, 43], we develop the *topological nonlinear Kirchhoff conditions algorithm*, a generalization of Kirchhoff's current and voltage laws (Fig. 1). Most previous studies have focused on simplicial complexes, yet many real-world structures, such as architectural trusses, social interactions or protein complexes, are better described as cell complexes [21, 44–46], comprised of larger polyhedral faces. Despite their prevalence, the study of dynamical phenomena on cell complexes is still in its infancy.

Our algorithm systematically identifies all distinct phase-synchronized states in cell complexes and provides rigorous criteria for when going beyond pairwise interactions pays off in terms of multistability. We demonstrate our approach on three minimal but paradigmatic classes of cell complexes: (i) rings, (ii) Platonic solids, and (iii) simplexes. These basic motifs can be combined to build larger complexes with potentially even richer multistability. Our framework can be applied to any dimension, but we focus on the case most relevant to applications, where the dynamics is defined on edges and interactions occur via nodes and faces [46].

In summary, we show that cell complexes support richer multistability than simplicial complexes of the same dimension. Higher-order connectivity gives rise to structural cascades in which stable states are inherited across dimensions. We also find indications of universality classes due to boundary structure.

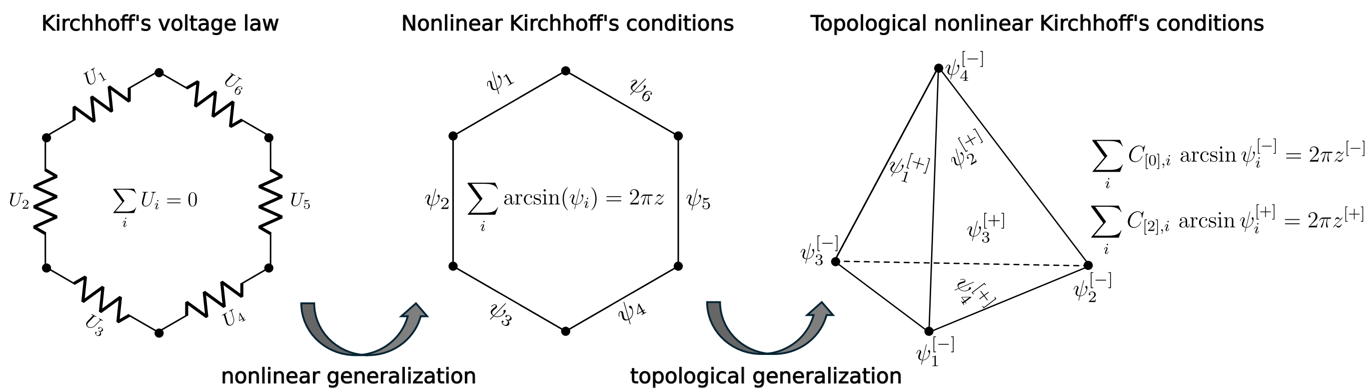

FIG. 1. *From Kirchhoff's circuit law to the topological nonlinear Kirchhoff conditions.* Kirchhoff's voltage law enforces linear conservation of potential differences around each circuit loop. In the nonlinear generalization, phase differences ψ_i across network edges satisfy a nonlinear constraint, $\sum_i \arcsin(\psi_i) = 2\pi z$, where integer winding numbers z describe distinct phase-locked states. The topological generalization extends this principle to higher-order interactions on cell complexes, where linear combinations of nonlinear phase differences across higher-dimensional cells satisfy $\sum_i C_i \arcsin \psi_i^{[\pm]} = 2\pi z_i^{[\pm]}$, with C_i determined by the boundary structure of each cell. Here, the dynamics is defined on edges, and interactions occur via nodes in the lower dimension ($\psi_i^{[-]}$) and faces in the upper dimension ($\psi_i^{[+]}$).

II. CELL COMPLEXES

Cell complexes are generalised network structures that contain cells of different dimensions [12, 44, 45]. In addition to nodes ($n = 0$) and edges ($n = 1$) found in standard graphs, they can include polygons ($n = 2$), polytopes ($n = 3$) and other higher-dimensional elements. Most studies on synchronization focus on the special case of simplicial complexes [34, 36], where each cell is an Euclidean simplex, but many real-world systems are better described by cell complexes.

The boundary of an n-dimensional cell consists of a number of cells of dimension $n-1$, and cells of consecutive dimensions are linked by boundary operators. We denote a set of cells of dimension n by $S_{[n]}$, with $N_{[n]} = |S_{[n]}|$. We generally consider a complex of cells $S_{[n-1]}$, $S_{[n]}$, $S_{[n+1]}$, where each boundary of a cell in $S_{[n']}$ must be an element of $S_{[n'-1]}$ for every n'. For calculations, we introduce an algebraic representation where we label all cells $j \in S_{[n]}$ consecutively as $j = 1, 2, \ldots, N_{[n]}$ and represent each cell by the jth standard unit vector $\boldsymbol{u}_j \in \mathbb{R}^{N_{[n]}}$. Fixing an orientation of each cell, we can represent the boundary operator between $S_{[n]}$ and $S_{[n-1]}$ by a matrix $\boldsymbol{B}_{[n]} \in \mathbb{R}^{N_{[n-1]} \times N_{[n]}}$ with entries $+1$, -1 or 0.

We briefly recall several important properties of the boundary matrices. First, the boundary of a boundary is always empty, such that

$$\boldsymbol{B}_{[n]} \boldsymbol{B}_{[n+1]} = 0, \qquad \boldsymbol{B}_{[n+1]}^\top \boldsymbol{B}_{[n]}^\top = 0. \tag{1}$$

Using this property, one can show that every vector $\boldsymbol{x}_{[n]} \in \mathbb{R}^{N_{[n]}}$ can be decomposed according to the Hodge decomposition [47] as

$$\boldsymbol{x}_{[n]} = \boldsymbol{x}_{[n]}^H + \boldsymbol{B}_{[n]}^\top \boldsymbol{z}_{[n-1]} + \boldsymbol{B}_{[n+1]} \boldsymbol{z}_{[n+1]}, \tag{2}$$

where $\boldsymbol{x}_{[n]}^H$ is referred to as the harmonic component that satisfies $\boldsymbol{B}_{[n+1]}^\top \boldsymbol{x}_{[n]}^H = \boldsymbol{0}$ and $\boldsymbol{B}_{[n]} \boldsymbol{x}_{[n]}^H = \boldsymbol{0}$. This decomposition plays a central role in our analysis.

To study dynamics defined on such cell complexes, we define *phase* variables supported on n-dimensional cells. These phases are coupled via interactions occurring "from below" via $(n-1)$-dimensional boundaries and "from above", via the $(n+1)$-dimensional cells. For example, for $n = 1$, edges can interact if they share a node, or if they are part of the same polygonal face. Two illustrative examples are shown in Fig. 2. The first is a hexagon, whose boundary consists of six edges ($n = 1$), each of which has a boundary of two nodes ($n = 0$). The second is a cube, with boundaries consisting of the six faces ($n = 2$), 12 edges ($n = 1$) and 8 nodes ($n = 0$). Ordinary graphs are recovered for $n = 0$, where only pairwise interactions exist. Including group interactions in cell complexes with $n \geq 1$ allows one to describe a much richer variety of dynamical systems.

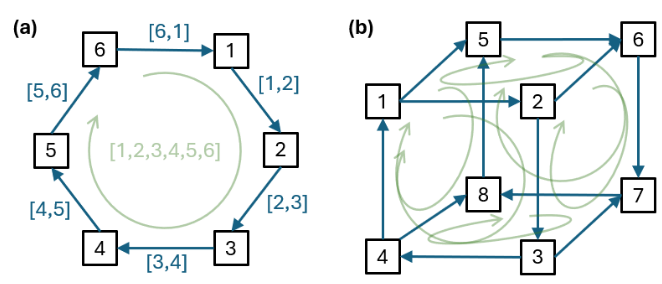

FIG. 2. *Examples of cell complexes for $n = 1$.* Two representative cell complexes, (a) a ring and (b) a cube, where the dynamics is defined on the edges, and interactions occur via both nodes and faces. Nodes are shown in black, edges in blue and faces in light green.

III. PHASE LOCKING IN THE TOPOLOGICAL KURAMOTO MODEL

In this article we consider a generalized topological Kuramoto model [34] allowing for inhomogeneous coupling constants. The basic dynamic variables are the phases $\theta_i(t)$ associated to each n-dimensional cell. These phases interact via cells of lower and higher dimension. In the case $n=1$ for example, phases are defined for each edge, and interact via vertices and faces. Summarizing the dynamical variables in the vector $\boldsymbol{\theta} = \left(\theta_1, \dots \theta_{N_{[n]}}\right)^\top$, the equations of motion read

$$\begin{aligned}\frac{d\boldsymbol{\theta}}{dt} &= \boldsymbol{\omega} - \boldsymbol{B}_{[n]}^\top \boldsymbol{K}_{[n]} \sin\left(\boldsymbol{B}_{[n]}\boldsymbol{\theta}\right) \\ &\quad - \boldsymbol{B}_{[n+1]}\boldsymbol{K}_{[n+1]} \sin\left(\boldsymbol{B}_{[n+1]}^\top \boldsymbol{\theta}\right), \end{aligned} \tag{3}$$

where $\boldsymbol{\omega}$ is the vector of the natural frequencies. The matrices $\boldsymbol{K}_{[n]}$ and $\boldsymbol{K}_{[n+1]}$ are diagonal and summarize positive coupling constants. In the case $n=0$ the coupling constants correspond to edge weights. The original topological Kuramoto model is recovered by setting $\boldsymbol{K}_{[n]} = \sigma\mathbb{1}$ and $\boldsymbol{K}_{[n+1]} = \sigma\mathbb{1}$, where $\mathbb{1}$ is the identity matrix of the respective size. The standard Kuramoto model for weighted complex networks is recovered for $n=0$, with no interaction via the lower dimension.

We can decouple the dynamics by multiplying the equations of motion by $\boldsymbol{B}_{[n]}$ and $\boldsymbol{B}_{[n+1]}^\top$ from the left [34]. Defining the variables

$$\boldsymbol{\theta}^{[+]} = \boldsymbol{B}_{[n+1]}^\top \boldsymbol{\theta}, \quad \text{and} \quad \boldsymbol{\theta}^{[-]} = \boldsymbol{B}_{[n]}\boldsymbol{\theta}, \tag{4}$$

we obtain the decoupled equations

$$\frac{d\boldsymbol{\theta}^{[+]}}{dt} = \boldsymbol{B}_{[n+1]}^\top \boldsymbol{\omega} - \boldsymbol{L}_{[n+1]}^{[down]} \boldsymbol{K}_{[n+1]} \sin\left(\boldsymbol{\theta}^{[+]}\right) \tag{5}$$

$$\frac{d\boldsymbol{\theta}^{[-]}}{dt} = \boldsymbol{B}_{[n]}\boldsymbol{\omega} - \boldsymbol{L}_{[n-1]}^{[up]} \boldsymbol{K}_{[n]} \sin\left(\boldsymbol{\theta}^{[-]}\right) \tag{6}$$

with the Laplacian matrices

$$\boldsymbol{L}_{[n-1]}^{[up]} = \boldsymbol{B}_{[n]}\boldsymbol{B}_{[n]}^\top, \qquad \boldsymbol{L}_{[n+1]}^{[down]} = \boldsymbol{B}_{[n+1]}^\top \boldsymbol{B}_{[n+1]}. \tag{7}$$

Here, we analyze the phase locked states of the topological Kuramoto model. Setting the time derivatives to zero, we get the conditions

$$\boldsymbol{B}_{[n+1]}^\top \boldsymbol{\omega} = \boldsymbol{L}_{[n+1]}^{[down]} \boldsymbol{K}_{[n+1]} \sin\left(\boldsymbol{\theta}^{[+]}\right) \tag{8}$$

$$\boldsymbol{B}_{[n]}\boldsymbol{\omega} = \boldsymbol{L}_{[n-1]}^{[up]} \boldsymbol{K}_{[n]} \sin\left(\boldsymbol{\theta}^{[-]}\right). \tag{9}$$

The stability of phase locking can be determined from the Jacobian matrix of the equations of motion (3) given by

$$\begin{aligned}\boldsymbol{J} = &- \boldsymbol{B}_{[n]}^\top \boldsymbol{K}_{[n]} \mathrm{diag}\left[\cos\left(\boldsymbol{\theta}^{[-]}\right)\right] \boldsymbol{B}_{[n]} \\ &- \boldsymbol{B}_{[n+1]}\boldsymbol{K}_{[n+1]} \mathrm{diag}\left[\cos\left(\boldsymbol{\theta}^{[+]}\right)\right] \boldsymbol{B}_{[n+1]}^\top. \end{aligned} \tag{10}$$

In general, a stationary state is linearly stable if the real part of all eigenvalues is negative [48]. If the stationary state satisfies the conditions

$$\cos\left(\boldsymbol{\theta}^{[-]}\right) > 0 \quad \text{and} \quad \cos\left(\boldsymbol{\theta}^{[+]}\right) > 0 \tag{11}$$

we find that all eigenvalues are real and satisfy the following conditions: (i) If an eigenvector $\boldsymbol{v}$ is purely harmonic, then the associated eigenvalue is given by $\lambda = 0$. (ii) If an eigenvector $\boldsymbol{v}$ is not purely harmonic, then the associated eigenvalue satisfies $\lambda < 0$ (see appendix for a proof). We thus conclude that a stationary state that satisfies Eq. (11) is linearly stable with respect to perturbations that are orthogonal to the harmonic subspace and neutrally stable with respect to harmonic perturbations. Since harmonic perturbations do not affect the projected quantities $\boldsymbol{\theta}^{[+]}$ and $\boldsymbol{\theta}^{[-]}$, phase locking is linearly stable.

In the following we will mainly concentrate on phase locked states that satisfy the conditions in Eq. (11) and refer to them as normal fixed points. Stationary states that violate Eq. (11) are typically, but not always, linearly unstable. For the ordinary Kuramoto model $n=0$, it has been shown that stable phase locked states that violate these conditions exist at the border of the stability region [49]. We will return to this question later in the context of polygonal face complexes, where we find such stable phase-locked states that aren't normal fixed points (Fig.3).

IV. THE TOPOLOGICAL NONLINEAR KIRCHHOFF CONDITIONS

Next, we introduce a two-step approach to explore phase locking: In the first step, we generate a space of solution candidates determined by a linear set of equations. In the second step, the actual solutions are singled out by a nonlinear condition. These two steps generalize Kirchhoff's current law and Kirchhoff's voltage law from circuits theory, as we will discuss in detail below.

We first define the auxiliary variables

$$\boldsymbol{\psi}^{[\pm]} = \sin\left(\boldsymbol{\theta}^{[\pm]}\right). \tag{12}$$

In the case $n=1$, the original dynamical variables $\boldsymbol{\theta}$ are defined on the edges of the cell complex, while the variables $\boldsymbol{\psi}^{[+]}$ are defined on the faces, and the variables $\boldsymbol{\psi}^{[-]}$ on the nodes. In the case $n=0$, the original dynamical variables $\boldsymbol{\theta}$ are defined on the nodes of the graph, while the auxiliary variables $\boldsymbol{\psi}^{[+]}$ are defined on its edges. In the theory of supply networks, the entries of $\boldsymbol{K}_{[1]}\boldsymbol{\psi}^{[+]}$ are interpreted as flows [50–52].

We then construct the solution candidates in terms of the auxiliary variables. The equations (9) read

$$\boldsymbol{B}_{[n+1]}^\top \boldsymbol{\omega} = \boldsymbol{L}_{[n+1]}^{[down]} \boldsymbol{K}_{[n+1]} \boldsymbol{\psi}^{[+]} \tag{13}$$

$$\boldsymbol{B}_{[n]}\boldsymbol{\omega} = \boldsymbol{L}_{[n-1]}^{[up]} \boldsymbol{K}_{[n]} \boldsymbol{\psi}^{[-]}. \tag{14}$$

If we treat the $\boldsymbol{\psi}^{[\pm]}$ as free variables, the solutions to this linear set of Eqs. (13) and (14) define a low-dimensional affine linear subspace.

To parametrize the set of solution candidates, we need the kernel of the matrices $\boldsymbol{B}_{[n+1]}$ and $\boldsymbol{B}_{[n]}^\top$. We compute a basis of these kernels and store the basis vectors as columns of the matrices $\boldsymbol{C}_{[n+1]}$ and $\boldsymbol{C}_{[n]}^\top$, respectively. We thus have

$$\boldsymbol{B}_{[n+1]}\boldsymbol{C}_{[n+1]} = \boldsymbol{0}, \qquad \boldsymbol{B}_{[n]}^\top \boldsymbol{C}_{[n]}^\top = \boldsymbol{0}. \tag{15}$$

Note that these matrices are intimately related, but not identical to the matrices $\boldsymbol{B}_{[n+2]}$ and $\boldsymbol{B}_{[n-1]}^\top$ via Eq. (1). The columns of the matrix $\boldsymbol{B}_{[n+2]}$ ($\boldsymbol{B}_{[n-1]}^\top$) lie in the kernel of $\boldsymbol{B}_{[n+1]}$ ($\boldsymbol{B}_{[n]}^\top$), but the kernel also contains the harmonic vectors. Having constructed the kernel, we can write the solutions of Eqs. (13) and (14) as

$$\begin{aligned}\boldsymbol{\psi}^{[+]} &= \boldsymbol{\psi}_{\rm sp}^{[+]} + \boldsymbol{K}_{[n+1]}^{-1}\boldsymbol{C}_{[n+1]}\boldsymbol{\zeta}^{[+]},\\ \boldsymbol{\psi}^{[-]} &= \boldsymbol{\psi}_{\rm sp}^{[-]} + \boldsymbol{K}_{[n]}^{-1}\boldsymbol{C}_{[n]}^\top\boldsymbol{\zeta}^{[-]},\end{aligned} \tag{16}$$

where $\boldsymbol{\zeta}^{[\pm]}$ are vectors of free coefficients which parametrize the homogeneous solution space, such that different choices of $\boldsymbol{\zeta}^{[\pm]}$ provide different candidate solutions. The particular solutions $\boldsymbol{\psi}_{\rm sp}^{[\pm]}$ can be calculated by applying the Moore–Penrose pseudoinverse to Eqs. (13)-(14) such that

$$\begin{aligned}\boldsymbol{\psi}_{\rm sp}^{[+]} &= \left(\boldsymbol{L}_{[n+1]}^{[down]}\boldsymbol{K}_{[n+1]}\right)^\dagger \boldsymbol{B}_{[n+1]}^\top\boldsymbol{\omega} = \boldsymbol{K}_{[n+1]}^{-1}\boldsymbol{B}_{[n+1]}^\dagger\boldsymbol{\omega}\\ \boldsymbol{\psi}_{\rm sp}^{[-]} &= \left(\boldsymbol{L}_{[n-1]}^{[up]}\boldsymbol{K}_{[n]}\right)^\dagger \boldsymbol{B}_{[n]}\boldsymbol{\omega} = \boldsymbol{K}_{[n]}^{-1}\boldsymbol{B}_{[n]}^{\dagger\top}\boldsymbol{\omega}\end{aligned} \tag{17}$$

This corresponds to the least squares solution of the linear system given by Eqs. (13)- (14).

Therefore, $\psi^{[\pm]} = 0$ if $\boldsymbol{\omega} = 0$. Furthermore, the auxiliary variables must satisfy the inequalities

$$|\boldsymbol{\psi}^{[\pm]}| \le 1, \tag{18}$$

since all variables are defined via sine functions. Hence, the set of solution candidates is given by the intersections of a low dimensional affine subspace and the unit cube. The intersection can be empty depending on $\boldsymbol{\omega}$.

The complexity of finding a stationary state is then shifted to the question of whether a solution candidate (16) exists that can be expressed as (12). To approach this topic, we first discuss how to recover the original variables $\boldsymbol{\theta}^{[\pm]}$ from the $\boldsymbol{\psi}^{[\pm]}$. If the equations Eq. (12) have solutions, they can have the form $\arcsin(\cdot)$ or $\pi - \arcsin(\cdot)$.

To keep track of the two options, we partition the sets of cells $S_{[n+1]}$ and $S_{[n-1]}$ into two parts depending on the value of $\cos\left(\theta_i^{[\pm]}\right)$. If the cosine is positive we define the inverse

$$f^\bullet(\psi_i^{[\pm]}) = \arcsin(\psi_i^{[\pm]}) \tag{19}$$

up to integer multiples of 2π and collect the respective cells in the sets $S_{[n+1]}^\bullet$ and $S_{[n-1]}^\bullet$. Likewise, if the cosine is not positive, we define the inverse

$$f^\circ(\psi_i^{[\pm]}) = \pi - \arcsin(\psi_i^{[\pm]}) \tag{20}$$

up to integer multiples of 2π and collect the respective cells in the sets $S_{[n+1]}^\circ$ and $S_{[n-1]}^\circ$. Finally, we summarize the resulting components in the two vector-valued functions $\boldsymbol{f}_{[n+1]}(\boldsymbol{\psi}^{[+]})$ and $\boldsymbol{f}_{[n-1]}(\boldsymbol{\psi}^{[-]})$.

The question whether a solution candidate (16) exists that can be expressed as (12) can thus be formulated as

$$\begin{aligned}\boldsymbol{f}_{[n+1]}(\boldsymbol{\psi}^{[+]}) &\in \text{image}\left(\boldsymbol{B}_{[n+1]}^\top\right),\\ \boldsymbol{f}_{[n-1]}(\boldsymbol{\psi}^{[-]}) &\in \text{image}\left(\boldsymbol{B}_{[n]}\right),\end{aligned} \tag{21}$$

up to integer multiples of 2π. A vector is in the image of a matrix if it is orthogonal to the kernel of the transpose matrix. We thus have the conditions

$$\begin{aligned}\boldsymbol{C}_{[n+1]}^\top\boldsymbol{f}_{[n+1]}(\boldsymbol{\psi}^{[+]}) &= 2\pi\boldsymbol{z}^{[+]},\\ \boldsymbol{C}_{[n]}\boldsymbol{f}_{[n-1]}(\boldsymbol{\psi}^{[-]}) &= 2\pi\boldsymbol{z}^{[-]},\end{aligned} \tag{22}$$

where $\boldsymbol{z}^{[\pm]}$ is a vector of integers. In the case of ordinary graphs, the vectors $\boldsymbol{z}^{[\pm]}$ are referred to as winding vectors and its components as winding numbers [7–9]. We will adopt this notation in the following and discuss the interpretation below.

To summarize, we propose the following algorithm to compute phase locked states of the topological Kuramoto model.

Algorithm 1 (Topological nonlinear Kirchhoff conditions)**.** *To compute the phase locked states of the topological Kuramoto model (Eq.* (3)*):*

1. *Parametrize the set of solutions candidates as* (16) *while taking into account the constraints* $|\boldsymbol{\psi}^{[\pm]}| \le 1$.
2. *Choose a partition* $S_{[n+1]} = S_{[n+1]}^\bullet \cup S_{[n+1]}^\circ$ *and* $S_{[n-1]} = S_{[n-1]}^\bullet \cup S_{[n-1]}^\circ$.
3. *Find the solutions of the set of equations* (22) *where* $\boldsymbol{z}^{[\pm]}$ *is a vector of integers.*
4. *Check the stability from the Jacobian* $\boldsymbol{J}$ *if necessary via Eq.* (10).

We briefly discuss three important aspects of this algorithmic approach to phase locking. First, phase locked states with $S^\circ = \emptyset$ are always linearly stable and as such are especially relevant for applications. States with $S^\circ \neq \emptyset$ are typically, but not always unstable. In fact, we will demonstrate the existence of stable phase locked states with $S^\circ \neq \emptyset$ close to bifurcations (cf. Fig. 4).

Second, the algorithm can be viewed as a topological, nonlinear generalization of Kirchhoff's circuit laws (Fig. 1). This is most easily see for the case of ordinary graphs $n=0$. Here, the entries of $\boldsymbol{K}_{[1]}\boldsymbol{\psi}^{[+]}$ are interpreted as flows or currents defined on edges [50–52]. The set of solution candidates obtained by Eq. (16) correspond to all states that satisfy Kirchhoff's current law at each node. These states can be decomposed into a special solution plus a set of loop flows. If we linearize the sine and arcsine functions and set $\boldsymbol{z}^{[\pm]}=\boldsymbol{0}$, then conditions (22) correspond to Kirchhoff's voltage law. Together, Kirchhoff's voltage and current laws then uniquely determine the currents.

Algorithm 1 introduces two generalizations: (i) The nonlinearity of the sine introduces multistability. Since $\sin(\alpha)=\sin(\alpha+2\pi z)$ for all $z\in\mathbb{Z}$, we can obtain different values for phase variables when inverting the sine function. Hence, we can obtain different solutions parametrized by the winding numbers z [7–9]. (ii) The algorithm generalizes the nonlinear Kirchhoff conditions to cell complexes of arbitrary dimensions.

Third, the possible values of the entries of the vectors $\boldsymbol{z}^{[\pm]}$ and thus the number of steady states is bounded depending on the topology of the cell complex. This bound is essentially determined by the number of of cells of higher or lower dimension that are adjacent to a given cell k. More precisely, let $m_k^{[+]}$ denote the number of cells of dimension $n+1$ in the boundary of the kth cell of dimension $n+2$ and $m_k^{[-]}$ the number of cells of dimension n that have the kth cell of dimension $n-1$ in its boundary. We then obtain the bounds

$$|z_k^{[+]}|\leq\frac{m_k^{[+]}}{4}\qquad\text{and}\qquad|z_k^{[-]}|\leq\frac{m_k^{[-]}}{4}.\tag{23}$$

for every k that does not corresponds to the harmonic component (see appendix for a proof). In the case of normal fixed points with $S^\circ=\emptyset$ we obtain a $<$ instead of the $\leq$. We conclude that we typically need $m_k^{[\pm]}\geq 5$ for multistability.

V. CLASS 1: POLYGONAL FACES

Polygons are among the simplest models of a cell complex, comprised of a single polygonal face bounded by its edges. We start by considering a ring of 6 vertices, 6 edges and 1 face as illustrated in Fig. 2a. Our main interest here will be dynamics of phases defined on the edges ($n=1$), which interact via the nodes ($n=0$) and face ($n=2$). In this example, we demonstrate our algorithm step-by-step, including the study of unstable states.

Denoting all cells by the vertices in the respective cell, we have

$$\begin{aligned}S_{[0]}&=\{[1],[2],[3],[4],[5],[6]\}\\S_{[1]}&=\{[1,2],[2,3],[3,4],[4,5],[5,6],[6,1]\}\\S_{[2]}&=\{[1,2,3,4,5,6]\}.\end{aligned}$$

The boundary operators are given in [53]. We find that the kernel of $\boldsymbol{B}_{[2]}$ is empty and the of the boundary operator $\boldsymbol{B}_{[1]}^\top$ is spanned by the harmonic vector $\mathbf{1}$. Hence, the set of solutions candidates (16) is given by

$$\boldsymbol{\psi}^{[+]}=\boldsymbol{\psi}_{\rm sp}^{[+]},\qquad\boldsymbol{\psi}^{[-]}=\boldsymbol{\psi}_{\rm sp}^{[-]}+\boldsymbol{K}_{[1]}^{-1}\mathbf{1}\,\zeta^{[-]}.\tag{24}$$

The phase conditions (22) reduce to

$$\mathbf{1}^\top\boldsymbol{f}_{[n-1]}(\boldsymbol{\psi}^{[-]})=2\pi\boldsymbol{z}^{[-]}.\tag{25}$$

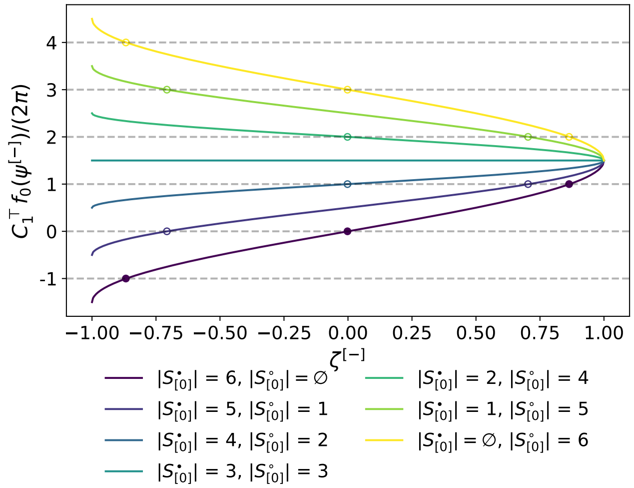

FIG. 3. *Phase locked solutions of the topological Kuramoto model for a six-edge ring.* Each marker represents a distinct phase-locked solution obtained from the nonlinear Kirchhoff conditions. Filled (empty) markers indicate linearly stable (unstable) solutions. Every partition except $|S^\bullet_{[0]}|=|S^\circ_{[0]}|=3$ gives rise to phase-locked solutions. For $|S^\bullet_{[0]}|=6,|S^\circ_{[0]}|=0$, three distinct stable phase-locked solutions coexist, illustrating multistability in the minimal ring motif.

We start by exploring the fully symmetric case when $\boldsymbol{\omega}=0$, due to which $\boldsymbol{\psi}^{[+]}=0$ and $\boldsymbol{\psi}_{\rm sp}^{[-]}=0$. In Fig. 3 we plot the expression $\mathbf{1}^\top\boldsymbol{f}_{[n-1]}(\boldsymbol{\psi}^{[-]})/(2\pi)$ as a function of the parameter $\zeta^{[-]}$, for each of the partitions $S_{[0]}=S^\bullet_{[0]}\cup S^\circ_{[0]}$. Since there are six elements that can either be $\bullet$ or $\circ$, we obtain 64 different partitions of $S_{[0]}$. Due to symmetry, these 64 curves in Fig. 3 are grouped according to the 7 different multiset permutations (i.e. fixed size of both partitions). Phase locked states are found where the curves cross an integer value. All of the partitions, except those where $|S^\bullet_{[0]}|=|S^\circ_{[0]}|=3$ provide phase locked solutions for $\boldsymbol{\omega}=0$. Finally, after checking the stability of each of the phase-locked solutions, we find multistability for the all-normal partition $|S^\bullet_{[0]}|=6,|S^\circ_{[0]}|=0$, where three stable solutions coexist. All other solutions are unstable.

Next, we consider the effect of asymmetry in natural frequencies on the existence of solutions, $\boldsymbol{\omega}\neq\mathbf{0}$. Hereby we limit our exploration to two partitions, $S^\circ_{[0]}=\emptyset$, and $S^\circ_{[0]}=[5,6]$, with $\boldsymbol{\omega}=(0,0,0,0,+\omega_0,-\omega_0)$. We plot the phase conditions (25) divided by 2π as a function of $\zeta^{[-]}$

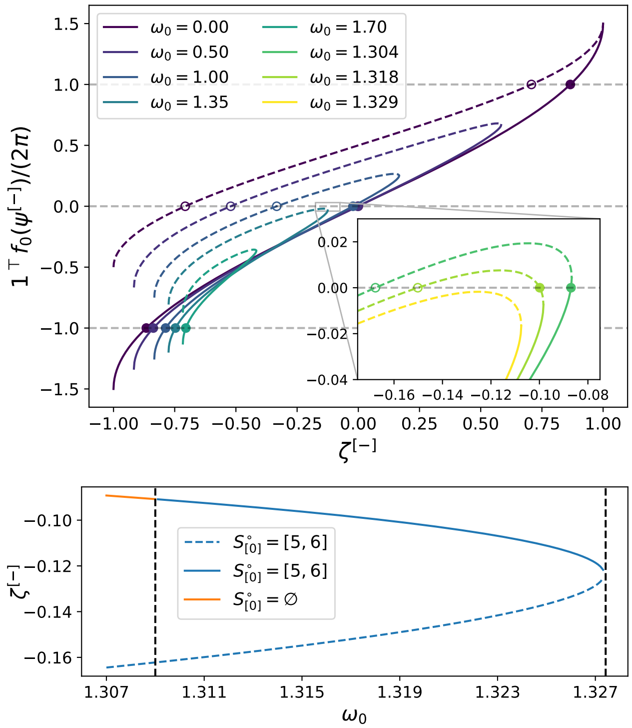

FIG. 4. *Effect of asymmetry in natural frequencies on stable phase-locked solutions in the ring with six edges.* Top row: Plots of condition (25) for two node partitions, $S^\circ_{[0]} = \emptyset$ (solid lines) and $S^\circ_{[0]} = [5, 6]$ (dashed lines) at selected values of ω_0 in $\boldsymbol{\omega} = (0, 0, 0, 0, \omega_0, -\omega_0)$. Filled (empty) symbols mark stable (unstable) solutions. The number of intersections with integer values decreases as ω_0 increases, i.e. phase locked states gradually disappear. The inset highlights a narrow interval of ω_0 where $S^\circ_{[0]} = [5, 6]$ crosses zero twice, producing one stable and one unstable solution, while $S^\circ_{[0]} = \emptyset$ does not cross it. Bottom row: Dependence of the corresponding phase-locked states on ω_0. The stable solution $S^\circ_{[0]} = \emptyset$ (orange line) vanishes near $\omega_0 \approx 1.309$, giving rise to the stable solution $S^\circ_{[0]} = [5, 6]$ (solid blue line). Stable and unstable (dashed blue line) solutions of $S^\circ_{[0]} = [5, 6]$ annihilate in a saddle-node bifurcation near $\omega_0 \approx 1.327$.

for chosen ω_0 values in Fig. 4. As before, we find that the former partitioning always gives rise to stable solutions, while the latter typically yields unstable ones. However, near the bifurcation point, the phase-locked state $S^\circ_{[0]} = \emptyset$ becomes $S^\circ_{[0]} = [5, 6]$ without losing stability. Increasing ω_0 further, the stable $S^\circ_{[0]} = [5, 6]$ solution annihilates with another unstable $S^\circ_{[0]} = [5, 6]$ solution in a saddle-node bifurcation. This scenario is shown in the bottom panel of Fig. 4.

Finally, let us generalize our result to polygonal faces of arbitrary size. We consider only the all-normal partitions $S^\bullet_{[0]} = S_{[0]}$ with $\boldsymbol{\omega} = 0$. If the ring size is $s = N_{[0]} = N_{[1]} \geq 3$, the number of stable phased-locked solutions

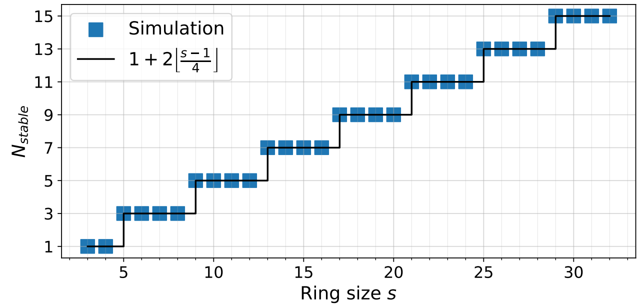

FIG. 5. *Dependence of the number of stable phase-locked states on ring size.* The number of stable solutions N_{stable} as a function of ring size s in an all-normal partitioned ring. Symbols show numerical results, and the solid line denotes the analytical prediction from Eq. (26).

N_{stable} increases with s as

$$N_{stable} = 1 + 2 \left\lfloor \frac{s-1}{4} \right\rfloor . \tag{26}$$

This is a consequence of Eq. (23). The solution with $z^{[-]} = 0$ always exists, and other solutions appear in pairs at integer values of $\pm z^{[-]}$, with jumps occurring at $\lfloor \frac{s-1}{4} \rfloor$, cf. Fig. 5, in line with previous results on the ordinary Kuramoto model [7].

VI. CLASS 2: PLATONIC SOLIDS

One might wonder what happens when several rings are combined together to create a polyhedron. We therefore now consider another class of elementary cell complexes: convex regular polyhedra in three-dimensional Euclidean space, also known as the Platonic solids. There are exactly five such objects: the tetrahedron, cube, octahedron, dodecahedron, and icosahedron (shown in Fig. 6). We will focus on the $n = 1$ case once again, where the dynamics on edges interacts via nodes and faces, and provide selected results for $n = 0$ and $n = 2$ at the end of the section.

For each cell complex, for $n = 1$, there are $2^{N_{[2]}} \cdot 2^{N_{[0]}}$ partitions of the sets $S_{[2]}$ and $S_{[0]}$. In larger polyhedra, the analysis of all partitions becomes exhaustive. We therefore limit ourselves in this section to the all-normal partition that provides stable normal solutions, $S^\bullet_{[2]} = S_{[2]}$ and $S^\bullet_{[0]} = S_{[0]}$. Moreover, we once again set $\boldsymbol{\omega} = \mathbf{0}$ as our default study case. The boundary matrices are given in [53].

Following algorithm 1 we first parametrize the set of solution candidates. We find that the kernels of the boundary operators are one-dimensional and spanned by the vectors $\mathbf{1}$ of appropriate dimension. For $\boldsymbol{\omega} = 0$, $\boldsymbol{K}_{[n]} = \mathrm{diag}(\mathbf{1}_{N_{[0]}})$ and $\boldsymbol{K}_{[n+1]} = \mathrm{diag}(\mathbf{1}_{N_{[2]}})$, the set of solution candidates (16) thus simplifies to

$$\boldsymbol{\psi}^{[+]} = \zeta^{[+]}\mathbf{1}$$
$$\boldsymbol{\psi}^{[-]} = \zeta^{[-]}\mathbf{1}.$$

Exploiting symmetry, the phase conditions (22) simplify to

$$N_{[2]} \arcsin \zeta^{[+]} = 2\pi z^{[+]}$$
$$N_{[0]} \arcsin \zeta^{[-]} = 2\pi z^{[-]}.$$

Hence, we finally obtain the solution

$$\boldsymbol{\psi}^{[+]} = \sin\left(\frac{2\pi z^{[+]}}{N_{[2]}}\right)\mathbf{1},$$
$$\boldsymbol{\psi}^{[-]} = \sin\left(\frac{2\pi z^{[-]}}{N_{[0]}}\right)\mathbf{1}.$$

We conclude that the normal phase-locked states on the edges $n = 1$ are determined by the number of nodes $N_{[0]}$ and faces $N_{[2]}$. We can further take into account the constraints on the winding numbers arising from Eq. (23) and find that $z^{[+]}$ can assume $N_{St,+} = 1 + 2\lfloor (N_{[2]} - 1)/4 \rfloor$ different values and $z^{[-]}$ can assume $N_{St,-} = 1 + 2\lfloor (N_{[0]} - 1)/4 \rfloor$ different values. All normal fixed points are parameterized by the Cartesian product of the winding numbers $z^{[+]}$ and $z^{[-]}$ such that their total number is given by

$$N_{stable} = N_{St,-} N_{St,+} = \left(1 + 2\left\lfloor \frac{N_{[0]} - 1}{4} \right\rfloor\right)\left(1 + 2\left\lfloor \frac{N_{[2]} - 1}{4} \right\rfloor\right). \tag{27}$$

From this, we immediately see that the tetrahedron with 4 vertices and 4 faces admits only one normal solution since $N_{St,-} = N_{St,+} = 1$. In other words, it is too small to generate multistability.

The larger the objects, the richer the multistability: the remaining four polyhedra admit respectively 9, 9, 45 and 45 coexisting stable solutions, as shown in Fig. 6. The curious result of coinciding numbers of stable solutions arises from the fact that the cube and octahedron, as well as the dodecahedron and icosahedron, are dual polyhedra: each vertex of one corresponds to a face of the other, and each edge connecting two vertices corresponds to the edge connecting the corresponding faces. Consequently, the product from Eq. (27) remains conserved, whereas the states themselves consist of exchanged positions in $(z^{[-]}, z^{[+]})$. Thus, objects that belong to the same symmetry group end up with the same universality pattern.

A detailed graphical exploration of the phase-locked solutions is shown in Fig. 6. The cascades of multistability inherited from both lower and higher dimensions become larger for larger objects. On the border of the stability region, we find marginally stable states which do not technically belong to the all-normal partition, since they satisfy $\cos \boldsymbol{\theta}^{[-]} = 0$.

Having presented the dynamically homogeneous $\boldsymbol{\omega} = \mathbf{0}$ case, let us demonstrate how tuning $\boldsymbol{\omega}$ allows us to control the cascade of multistability. We show this phenomenon on the smallest Platonic solid that admits multiple solutions, the cube. For $\boldsymbol{\omega} = \mathbf{0}$, the cube has 9 coexisting solutions (cf. Fig. 6). Upon introducing asymmetry to the vector of natural frequencies $\boldsymbol{\omega} = (0, 0, 0, 0, 0, 0, 0, 0, +\omega_0, 0, 0, +\omega_0)$, the number of stable fixed points decreases gradually, as shown in Fig. 7, disappearing in symmetric pairs or triplets (when a state with the winding number zero is included). In this case, there is no exchange of stability between different partitions as one finds in the ring. States with $S^\circ \neq \emptyset$ do not stabilize for any ω_0 value.

We conclude this section with a brief discussion for $n = 0$ and $n = 2$. For the tetrahedron, cube and octahedron, only a single stable solution exists, while for the dodecahedron and icosahedron, calculations become computationally prohibitive due to the combinatorial explosion of the number of possible solutions for winding number vectors. Nevertheless, the simpler cases already demonstrate the importance of including higher-order interactions for multistability in the topological Kuramoto model. Handling the combinatorial explosion poses an interesting problem for future work.

VII. CLASS 3: SIMPLEXES

In contrast to the cell complexes studied earlier, simplexes, especially in low dimensions, are far more limited in terms of multistability. The winding number constraint in Eq. (23) tells us that multistability will appear when there are more than 4 cells in the boundary. This is consistent with previously shown results for the 2-simplex (the triangle, or smallest ring, with three edges in the boundary) and 3-simplex (the tetrahedron, also the smallest Platonic solid, with four triangles in its boundary), each admitting only one stable solution for $n = 1$.

Here, we analyze the stable solutions of the all-normal partitions, $S^\bullet_{[2]} = S_{[2]}$ and $S^\bullet_{[0]} = S_{[0]}$, for all viable n values for simplexes up to 5 dimensions. For definiteness, we once again set $\boldsymbol{\omega} = 0$ and all couplings to unity. The explicit form of the boundary operators and the kernel matrices are given in [53]. Our results are summarized in Fig. 8. Note that whenever there is one stable solution, it refers to the trivial solution with winding number(s) zero. We list the winding number vectors for all stable solutions in all considered simplexes.

1. **The 2-simplex (triangle)** consists of 3 vertices and 3 edges. It supports the following stable states.
    - For $n = 0$, $z^{[+]} = 0$ with no lower dimension contribution.
    - For $n = 1$, $z^{[-]} = 0$ with no upper dimension contribution.

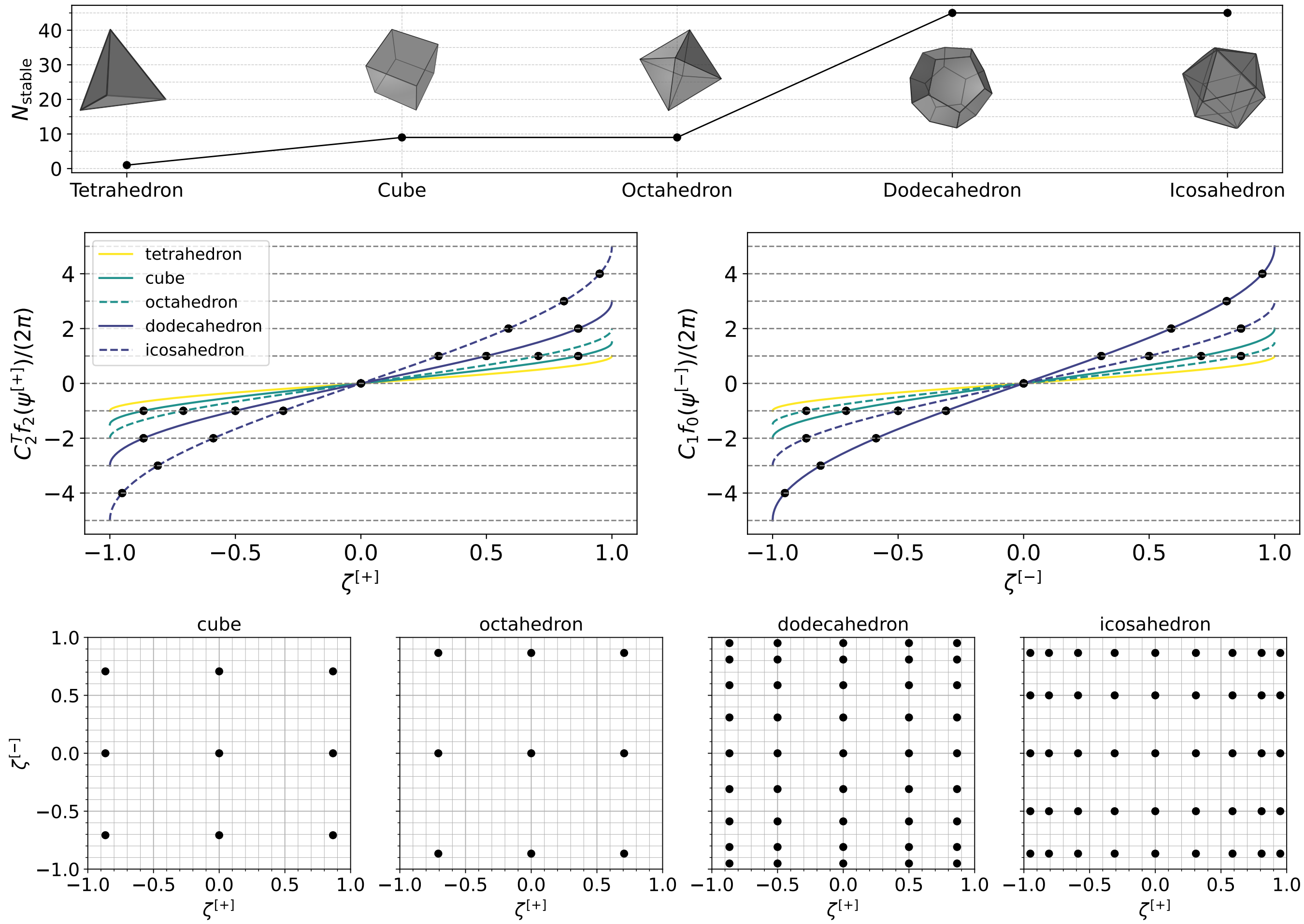

FIG. 6. *Multistability in Platonic solids (edge dynamics, $n = 1$).* Top row: number of stable phase-locked states N_{stable} for each Platonic solid (all-normal partition, $\boldsymbol{\omega} = 0$). Middle row: phase-locked solutions as solutions of the topological nonlinear Kirchhoff conditions Eq. (22) (black dots denote stable solutions). Other than the tetrahedron, all objects display structural cascades of multistability where stable states are inherited from both lower and higher dimensions. Dual Platonic solids are shown in matching colors with different line styles to emphasize their symmetry. Bottom row: stable phase-locked solutions in the $(\zeta^{[+]}, \zeta^{[-]})$ plane for the four solids that exhibit multistability.

2. **The 3-simplex (tetrahedron)** consists of 4 vertices, 6 edges and 4 triangular faces. It admits single stable states as follows.
    - For $n = 0$, $\boldsymbol{z}^{[+]} = (0, 0, 0)$ with no lower dimension contribution.
    - For $n = 1$, $z^{[-]} = 0$ and $z^{[+]} = 0$.
    - For $n = 2$, the upper dimension contributes with $\boldsymbol{z}^{[-]} = (0, 0, 0)$.
3. **The 4-simplex (5-cell)** consists of 5 vertices, 10 edges, 10 triangular faces, and 5 tetrahedra. We find the following stable states:
    - For $n = 0$, one stable state exists from the upper dimension, $\boldsymbol{z}^{[+]} = (0, 0, 0, 0, 0, 0)$.
    - For $n = 1$, the three stable states correspond to $\boldsymbol{z}^{[+]} = (0, 0, 0, 0)$ with $z^{[-]} \in \{0, \pm 1\}$.
    - For $n = 2$, three solutions exist with $z^{[+]} \in \{0, \pm 1\}$ and $\boldsymbol{z}^{[-]} = (0, 0, 0, 0)$.
    - For $n = 3$, a single solution comes from the lower dimension, with $\boldsymbol{z}^{[-]} = (0, 0, 0, 0, 0, 0)$.
4. **The 5-simplex** has 6 vertices, 15 edges, 20 triangular faces, 15 tetrahedral cells, and 6 5-cells in its outer boundary. It supports the following stable states.
    - For $n = 0$, $\boldsymbol{z}^{[+]} = (0, 0, 0, 0, 0, 0, 0, 0, 0, 0)$.
    - For $n = 1$, three solutions coexist: $\boldsymbol{z}^{[+]} = (0, 0, 0, 0, 0, 0, 0, 0, 0, 0)$ with $z^{[-]} \in \{0, \pm 1\}$.
    - For $n = 2$, there is only $\boldsymbol{z}^{[+]} = (0, 0, 0, 0, 0)$ with $\boldsymbol{z}^{[-]} = (0, 0, 0, 0, 0)$.
    - For $n = 3$, again three solutions coexist, $z^{[+]} \in \{0, \pm 1\}$ with $\boldsymbol{z}^{[-]} = (0, 0, 0, 0, 0, 0, 0, 0, 0, 0)$.

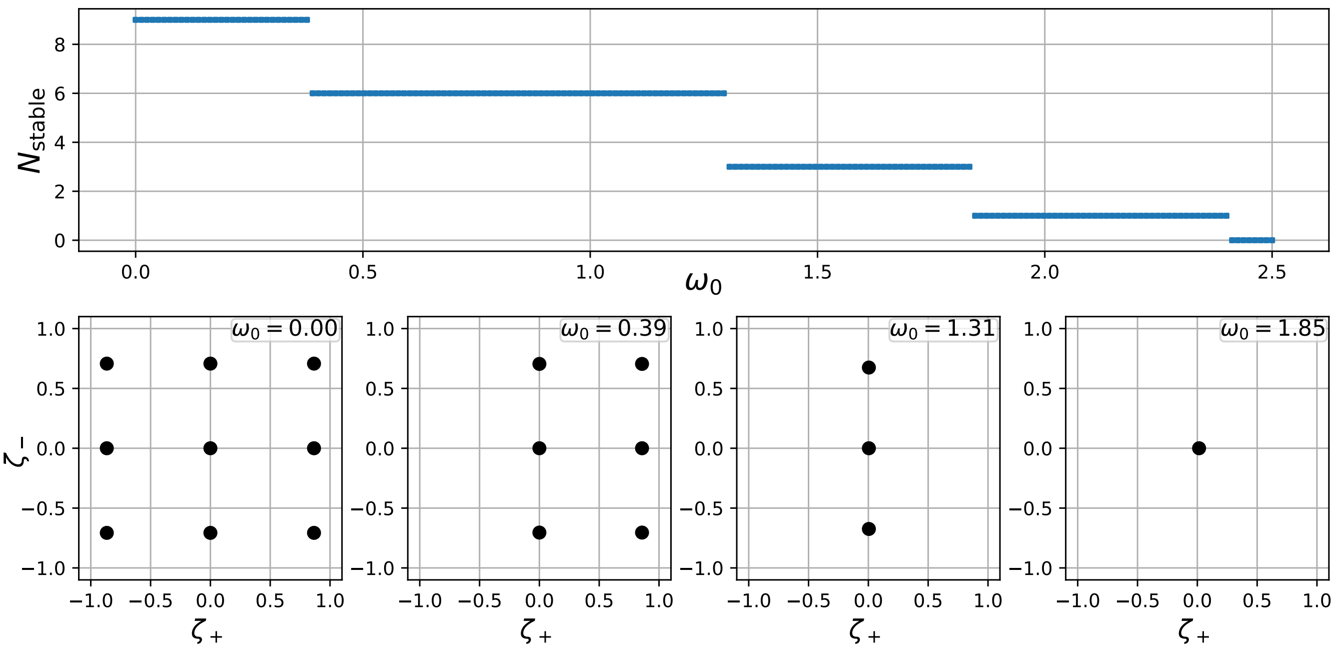

FIG. 7. *Reversal of the multistability cascade in the cube.* Gradual reduction in the number of stable fixed points for the all-normal partition of the cube as asymmetry is introduced into the vector of natural frequencies, $\boldsymbol{\omega} = (0,0,0,0,0,0,0,0,+\omega_0,0,0,+\omega_0)$. The plot shows how increasing ω_0 reverses the structural cascade of multistability observed in the symmetric case.

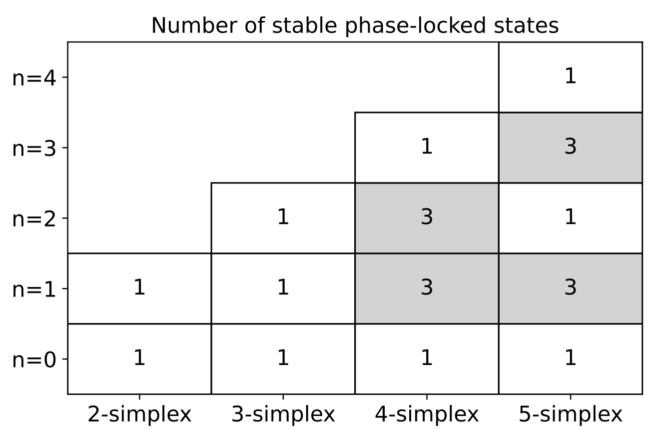

FIG. 8. *Number of stable phase-locked states in simplexes up to dimension 5.* For each cell dimension $n \in \{0, ..., d-1\}$, the number of stable (normal) phase-locked states obtained from the topological nonlinear Kirchhoff conditions with $\boldsymbol{\omega} = 0$ is shown. Multistability occurs only when at least one relevant boundary contains more than four cells; the 4-simplex is the smallest case satisfying this criterion. Pairs of n and d that exhibit multistability are highlighted in grey.

- For $n = 4$, we find only $\boldsymbol{z}^{[-]} = (0,0,0,0,0,0,0,0,0,0)$.

We can generalize our result on the dimension of $\boldsymbol{z}^{[\pm]}$ to simplexes of arbitrary dimension d and obtain

$$\dim \boldsymbol{z}^{[+]} = \dim \ker(\boldsymbol{B}_{n+1}) = \binom{d}{n+2}$$
$$\dim \boldsymbol{z}^{[-]} = \dim \ker(\boldsymbol{B}_n^\top) = \binom{d}{n-1} \tag{28}$$

with $\dim \boldsymbol{z}^{[-]} = 0$ for $n = 0$ (see appendix for a proof). The elements of $\boldsymbol{z}^{[\pm]}$ are integers. One can then apply the equations (23) to compute upper bounds for the number of allowed winding numbers. Deciding which vectors $\boldsymbol{z}^{[\pm]}$ are achievable is assisted by symmetry arguments: simplices with $\boldsymbol{\omega} = \mathbf{0}$ and equal coupling are symmetric to vertex permutations. Hence, if a certain $\boldsymbol{z}^{[\pm]}$ is achievable, then any permutation of its components, should also be achievable.

VIII. DISCUSSION

Our results establish a general theoretical framework for studying multistability in oscillator networks with higher-order interactions, integrating concepts from network science, geometry, and nonlinear dynamics. The topological nonlinear Kirchhoff conditions algorithm allows one to identify all phase-locked states of the topological Kuramoto model on arbitrary cell complexes. By applying it to minimal motifs (polygonal rings, Platonic solids, and simplexes), we showed that multistability emerges when boundaries contain more than four cells.

Structural cascades of multistability then arise, with stable states inherited from lower and/or upper dimensions. Moreover, dual Platonic solids display identical multistability patterns, suggesting the existence of universality classes determined by the boundary structure.

Future research could explore how these structural cascades manifest in heterogeneous systems, and how combining the elementary motifs studied here gives rise to multistability in larger complexes. Beyond theoretical interest, these findings are relevant for real-world systems where higher-order couplings are intrinsic, such as neuronal networks [11], optical and mechanical oscillator arrays [15, 54], power-grid stability [2, 55], and collective decision-making in multi-agent systems [56]. The framework may be applicable to other dynamical processes on cell complexes, including diffusion, consensus, and pattern-forming instabilities.

ACKNOWLEDGMENTS

We thank Ginestra Bianconi for stimulating discussion. D.W. and I.B. gratefully acknowledge support by the German Federal Ministry of Research, Technology and Space (Bundesministerium für Forschung, Technologie und Raumfahrt) via the grant number 03SF0751. M.T.S acknowledges support by the European Union (ERC, HIGH-HOPeS, 101039827). Views and opinions expressed are however those of the author(s) only and do not necessarily reflect those of the European Union or the European Research Council Executive Agency. Neither the European Union nor the granting authority can be held responsible for them.

Appendix A: Eigenvalues of the Jacobian

Let $\boldsymbol{v} \neq \boldsymbol{0}$ be an eigenvector of the Jacobian matrix $\boldsymbol{J}$ with associated eigenvalue λ such that

$$\boldsymbol{J}\boldsymbol{v} = \lambda \boldsymbol{v} \qquad \Rightarrow \qquad \lambda = \frac{\boldsymbol{v}^\top \boldsymbol{J} \boldsymbol{v}}{\boldsymbol{v}^\top \boldsymbol{v}} \,.$$

If $\boldsymbol{v}$ is purely harmonic then $\boldsymbol{B}_{[n]}\boldsymbol{v} = \boldsymbol{0}$ and $\boldsymbol{B}_{[n+1]}^\top \boldsymbol{v} = 0$ by definition and thus $\boldsymbol{J}\boldsymbol{v} = \boldsymbol{0} \Rightarrow \lambda = 0$. If $\boldsymbol{v}$ is not purely harmonic then $\boldsymbol{y}^{[-]} = \boldsymbol{B}_{[n]}\boldsymbol{v} \neq 0$ or/and $\boldsymbol{y}^{[+]} = \boldsymbol{B}_{[n+1]}^\top \boldsymbol{v} \neq 0$. We thus obtain

$$\begin{aligned}\lambda = &-(\boldsymbol{v}^\top \boldsymbol{v})^{-1} \Big\{ \boldsymbol{y}^{[-]\top} \boldsymbol{K}_{[n]} \mathrm{diag}\left[\cos\left(\bar{\boldsymbol{\theta}}^{[-]}\right)\right] \boldsymbol{y}^{[-]} \\ &\qquad + \boldsymbol{y}^{[+]\top} \boldsymbol{K}_{[n+1]} \mathrm{diag}\left[\cos\left(\bar{\boldsymbol{\theta}}^{[+]}\right)\right] \boldsymbol{y}^{[+]} \Big\} \\ = &-(\boldsymbol{v}^\top \boldsymbol{v})^{-1} \Big\{ \sum_j \left(y_j^{[-]}\right)^2 (K_{[n]})_{jj} \cos\left(\bar{\theta}_j^{[-]}\right) \\ &\qquad + \sum_j \left(y_j^{[+]}\right)^2 (K_{[n+1]})_{jj} \cos\left(\bar{\theta}_j^{[+]}\right) \Big\}.\end{aligned}$$

If the stationary state satisfies the conditions in Eq. (11), this implies $\lambda < 0$.

Appendix B: Proof of Eq. (23)

To proof Eq. (23), we rewrite Eq. (22) in components and use that $|f_\pm| \leq \pi/2$ and obtain

$$|z_k^{[+]}| = \frac{1}{2\pi} \left| \sum_i C_{[n+1],ik} f_\pm(\psi_i^{[+]}) \right| \leq \frac{1}{4} \sum_i |C_{[n+1],ik}|$$

$$|z_k^{[-]}| = \frac{1}{2\pi} \left| \sum_i C_{[n],ki} f_\pm(\psi_i^{[-]}) \right| \leq \frac{1}{4} \sum_i |C_{[n],ki}|.$$

In the case of normal fixed points with $S^\circ = \emptyset$ we obtain a $<$ instead of the $\leq$.

We recall that the matrices $\boldsymbol{C}$ are closely related to the boundary matrices. We can choose a basis of the kernel such that the kth column of $\boldsymbol{C}_{[n+1]}$ ($\boldsymbol{C}_{[n]}^\top$) is equal to the kth column of $\boldsymbol{B}_{[n+2]}$ ($\boldsymbol{B}_{[n-1]}^\top$) unless k corresponds to the harmonic component. A further simplification is possible by noting that the entries of the boundary matrix have the values $-1, 0, +1$. We then define $m_k^{[+]}$ as the number of non-zero elements of the kth column of $\boldsymbol{B}_{[n+2]}$ and $m_k^{[-]}$ as the number of non-zero elements of the kth row of $\boldsymbol{B}_{[n-1]}$. We then obtain the bounds given in Eq. (23)for every k that does not corresponds to the harmonic component.

Notably, the number of non-zero elements can be related to the number of adjacent cells and thus enables a geometric interpretation. The number $m_k^{[+]}$ counts the number of cells of dimension $n+1$ in the boundary of the kth cell of dimension $n+2$. The winding number $z_k^{[+]}$ counts how often the phases $\boldsymbol{\theta}^{[+]}$ wind by 2π when following all cells in this boundary. Likewise, the number $m_k^{[-]}$ counts the number of cells of dimension n that have the kth cell of dimension $n-1$ in its boundary.

Appendix C: Proof of equations (28)

We prove the equations (28) using a recurrence relation that is derived from the fact that d-simplex is contractible and the rank-nullity theorem. A d-simplex is contractible, which means that all homology groups are trivial except $H_0 \cong \mathbb{R}$,

$$H_n = 0, \quad n > 0, \tag{C1}$$

where a homology group is the quotient vector space

$$H_n = \frac{\ker \boldsymbol{B}_{[n]}}{\mathrm{im}\ \boldsymbol{B}_{[n+1]}} \tag{C2}$$

implying

$$\dim H_n = \dim \ker \boldsymbol{B}_{[n]} - \dim \mathrm{im}\ \boldsymbol{B}_{[n+1]}. \tag{C3}$$

Since $\boldsymbol{B}_{[n]}\boldsymbol{B}_{[n+1]} = 0$, every element in $\boldsymbol{B}_{[n+1]}$ lies in $\ker \boldsymbol{B}_{[n]}$,

$$\text{im } \boldsymbol{B}_{[n+1]} \subseteq \ker \boldsymbol{B}_{[n]} \tag{C4}$$

For $n > 0$, since $H_n = 0$, we have

$$\dim \ker \boldsymbol{B}_{[n]} = \dim \text{im } \boldsymbol{B}_{[n+1]} \tag{C5}$$

Combining Eqs. (C4) and (C5), we find for every $n > 0$

$$\text{im } \boldsymbol{B}_{[n+1]} = \ker \boldsymbol{B}_{[n]}. \tag{C6}$$

We now apply the rank nullity theorem to $\boldsymbol{B}_{[n]} : \mathbb{R}^{N_{[n]}} \to \mathbb{R}^{N_{[n-1]}}$ which yields

$$\dim \ker \boldsymbol{B}_{[n]} = N_{[n]} - \text{rank } \boldsymbol{B}_{[n]}. \tag{C7}$$

We thus obtain a recurrence relation valid for $n > 0$

$$N_{[n]} = \text{rank } \boldsymbol{B}_{[n+1]} + \text{rank } \boldsymbol{B}_{[n]} = \binom{d+1}{n+1}, \tag{C8}$$

where we used the fact that for a d-simplex, the number of n-dimensional faces, formed by choosing $n+1$ vertices from $d+1$ available ones, is $N_{[n]} = \binom{d+1}{n+1}$. Applying the recurrence relation for $n = d, \ldots, 1$ together with Pascal's identity then yields Eq. (28). As a last step, for $n = 0$, we have to slightly adapt the recurrence relation because

$$\dim H_0 = 1 = \dim \ker \boldsymbol{B}_{[0]} - \dim \text{im } \boldsymbol{B}_{[1]}. \tag{C9}$$

Nevertheless, this yields the same results as Eq. (28) for $\boldsymbol{z}^{[+]}$. Finally, there is no $\boldsymbol{z}^{[-]}$ for $n = 0$ which concludes the proof.

[1] A. Pikovsky, M. Rosenblum, and J. Kurths, *Synchronization: A Universal Concept in Nonlinear Sciences* (Cambridge University Press, 2001).

[2] F. Dörfler and F. Bullo, Synchronization in complex networks of phase oscillators: A survey, Automatica **50**, 1539 (2014).

[3] Y. Kuramoto, Self-entrainment of a population of coupled non-linear oscillators, in *International symposium on mathematical problems in theoretical physics: January 23–29, 1975, kyoto university, kyoto/Japan* (Springer, 1975) pp. 420–422.

[4] J. A. Acebrón, L. L. Bonilla, C. J. Pérez Vicente, F. Ritort, and R. Spigler, The kuramoto model: A simple paradigm for synchronization phenomena, Reviews of modern physics **77**, 137 (2005).

[5] S. H. Strogatz, From kuramoto to crawford: exploring the onset of synchronization in populations of coupled oscillators, Physica D: Nonlinear Phenomena **143**, 1 (2000).

[6] F. A. Rodrigues, T. K. D. Peron, P. Ji, and J. Kurths, The kuramoto model in complex networks, Physics Reports **610**, 1 (2016).

[7] D. Manik, M. Timme, and D. Witthaut, Cycle flows and multistability in oscillatory networks, Chaos: An Interdisciplinary Journal of Nonlinear Science **27**, 083123 (2017).

[8] R. Delabays, T. Coletta, and P. Jacquod, Multistability of phase-locking and topological winding numbers in locally coupled kuramoto models on single-loop networks, Journal of Mathematical Physics **57**, 032701 (2016).

[9] S. Jafarpour, E. Y. Huang, K. D. Smith, and F. Bullo, Flow and elastic networks on the n-torus: Geometry, analysis, and computation, SIAM Review **64**, 59 (2022).

[10] F. Hellmann, P. Schultz, P. Jaros, R. Levchenko, T. Kapitaniak, J. Kurths, and Y. Maistrenko, Network-induced multistability through lossy coupling and exotic solitary states, Nature communications **11**, 592 (2020).

[11] M. Breakspear, S. Heitmann, and A. Daffertshofer, Generative models of cortical oscillations: neurobiological implications of the Kuramoto model, Frontiers in Human Neuroscience **4**, 190 (2010).

[12] A. E. Sizemore, C. Giusti, A. Kahn, J. M. Vettel, R. F. Betzel, and D. S. Bassett, Cliques and cavities in the human connectome, Journal of Computational Neuroscience **44**, 115 (2018).

[13] C. Giusti, R. Ghrist, and D. S. Bassett, Two's company, three (or more) is a simplex: Algebraic-topological tools for understanding higher-order structure in neural data, Journal of Computational Neuroscience **41**, 1 (2016).

[14] M. Andjelković, B. Tadić, and R. Melnik, The topology of higher-order complexes associated with brain hubs in human connectomes, Scientific Reports **10**, 17320 (2020).

[15] M. Nixon, E. Ronen, A. A. Friesem, and N. Davidson, Observing geometric frustration with thousands of coupled lasers, Physical Review Letters **110**, 184102 (2013).

[16] E. Estrada and G. J. Ross, Centralities in simplicial complexes. applications to protein interaction networks, Journal of Theoretical Biology **438**, 46 (2018).

[17] A. P. Millán, H. Sun, L. Giambagli, R. Muolo, T. Carletti, J. J. Torres, F. Radicchi, J. Kurths, and G. Bianconi, Topology shapes dynamics of higher-order networks, Nature Physics **21**, 353 (2025).

[18] F. Battiston, G. Cencetti, I. Iacopini, V. Latora, M. Lucas, A. Patania, J.-G. Young, and G. Petri, Networks beyond pairwise interactions: Structure and dynamics, Physics reports **874**, 1 (2020).

[19] F. Battiston, E. Amico, A. Barrat, G. Bianconi, G. Ferraz de Arruda, B. Franceschiello, I. Iacopini, S. Kéfi, V. Latora, Y. Moreno, *et al.*, The physics of higher-order interactions in complex systems, Nature Physics **17**, 1093 (2021).

[20] G. Bianconi, *Higher-Order Networks: An Introduction to Simplicial Complexes* (Cambridge University Press, 2021).

[21] D. Mulder and G. Bianconi, Network geometry and com-

plexity, Journal of Statistical Physics **173**, 783 (2018).
[22] C. Bick, T. Gross, H. A. Harrington, and M. T. Schaub, What are higher-order networks?, SIAM Review **65**, 686 (2023).
[23] I. Iacopini, G. Petri, A. Barrat, and V. Latora, Simplicial models of social contagion, Nature Communications **10**, 2485 (2019).
[24] A. Santoro, F. Battiston, M. Lucas, G. Petri, and E. Amico, Higher-order connectomics of human brain function reveals local topological signatures of task decoding, individual identification, and behavior, Nature Communications **15**, 10244 (2024).
[25] Y. Zhang, M. Lucas, and F. Battiston, Higher-order interactions shape collective dynamics differently in hypergraphs and simplicial complexes, Nature Communications **14**, 1605 (2023).
[26] D. Horak, S. Maletić, and M. Rajković, Persistent homology of complex networks, Journal of Statistical Mechanics: Theory and Experiment **2009**, P03034 (2009).
[27] G. Petri, M. Scolamiero, I. Donato, and F. Vaccarino, Topological strata of weighted complex networks, PLoS One **8**, e66506 (2013).
[28] G. Petri, P. Expert, F. Turkheimer, R. L. Carhart-Harris, D. Nutt, P. J. Hellyer, and F. Vaccarino, Homological scaffolds of brain functional networks, Journal of The Royal Society Interface **11**, 20140873 (2014).
[29] Z. Wu, G. Menichetti, C. Rahmede, and G. Bianconi, Emergent complex network geometry, Scientific Reports **5**, 10073 (2015).
[30] M. Andjelković, B. Tadić, M. Mitrović Dankulov, M. Rajković, and R. Melnik, Topology of innovation spaces in the knowledge networks emerging through questions-and-answers, PLOS ONE **11**, e0154655 (2016).
[31] L. Calmon, S. Krishnagopal, and G. Biancon, Local dirac synchronization on networks, Chaos **33**, 033117 (2023).
[32] L. Calmon, J. G. Restrepo, J. J. Torres, and G. Bianconi, Dirac synchronization is rhythmic and explosive, Communications Physics **5**, 253 (2022).
[33] L. Calmon, M. T. Schauband, and G. Bianconi, Dirac signal processing of higher-order topological signals, New Journal of Physics **25**, 093013 (2023).
[34] A. P. Millán, J. J. Torres, and G. Bianconi, Explosive higher-order kuramoto dynamics on simplicial complexes, Physical Review Letters **124**, 218301 (2020).
[35] R. Ghorbanchian, J. G. Restrepo, J. J. Torres, and G. Bianconi, Higher-order simplicial synchronization of coupled topological signals, Communications Physics **4**, 120 (2021).
[36] M. Nurisso, A. Arnaudon, M. Lucas, R. L. Peach, P. Expert, F. Vaccarino, and G. Petri, A unified framework for simplicial kuramoto models, Chaos **34**, 053118 (2024).
[37] P. S. Skardal and A. Arenas, Higher order interactions in complex networks of phase oscillators promote abrupt synchronization switching, Communications Physics **3**, 218 (2020).
[38] M. Lucas, G. Cencetti, and F. Battiston, Multiorder laplacian for synchronization in higher-order networks, Physical Review Research **2**, 033410 (2020).
[39] T. Carletti, L. Giambagli, and G. Bianconi, Global topological synchronization on simplicial and cell complexes, Physical review letters **130**, 187401 (2023).
[40] P. S. Skardal and A. Arenas, Abrupt desynchronization and extensive multistability in globally coupled oscillator simplexes, Physical Review Letters **122**, 248301 (2019).
[41] L. DeVille, Consensus on simplicial complexes: Results on stability and synchronization, Chaos **31**, 023137 (2021).
[42] L. V. Gambuzza, F. D. Patti, L. Gallo, S. Lepri, M. Romance, R. Criado, M. Frasca, V. Latora, and S. Boccaletti, Stability of synchronization in simplicial complexes, Nature Communications **12**, 1255 (2021).
[43] F. Parastesh, M. Mehrabbeik, K. Rajagopal, S. Jafari, M. Perc, C. I. del Genio, and S. Boccaletti, Synchronization stability in simplicial complexes of near-identical systems, Physical Review Research **7**, 033039 (2025).
[44] J. Hoppe, V. P. Grande, and M. T. Schaub, Don't be afraid of cell complexes! an introduction from an applied perspective, arXiv preprint arXiv:2506.09726 (2025).
[45] T. M. Roddenberry, M. T. Schaub, and M. Hajij, Signal processing on cell complexes, in *IEEE International Conference on Acoustics, Speech and Signal Processing (ICASSP)* (2022) pp. 8852–8856.
[46] L. Giambagli, L. Calmon, R. Muolo, T. Carletti, and G. Bianconi, Diffusion-driven instability of topological signals coupled by the dirac operator, Physical Review E **106**, 064314 (2022).
[47] S. Barbarossa and S. Sardellitti, Topological signal processing over simplicial complexes, IEEE Transactions on Signal Processing **68**, 2992 (2020).
[48] S. H. Strogatz, *Nonlinear dynamics and chaos with student solutions manual: With applications to physics, biology, chemistry, and engineering* (CRC press, 2018).
[49] D. Manik, D. Witthaut, B. Schäfer, M. Matthiae, A. Sorge, M. Rohden, E. Katifori, and M. Timme, Supply networks: Instabilities without overload, The European Physical Journal Special Topics **223**, 2527 (2014).
[50] C. Hartmann, P. C. Böttcher, D. Gross, and D. Witthaut, Synchronized states of power grids and oscillator networks by convex optimization, PRX energy **3**, 043004 (2024).
[51] I. Bačić, C. Hartmann, P. C. Böttcher, D. Gross, A. Benigni, and D. Witthaut, Existence of phase-cohesive solutions of the lossless power-flow equations, TechRxiv Preprint DOI:10.36227/techrxiv.174611978.89382822/ (2025).
[52] A. Parameswaran, I. Bačić, A. Benigni, and D. Witthaut, Symmetry breaking in minimum dissipation networks, arXiv preprint arXiv:2505.24818 (2025).
[53] I. Bačić, Topological kuramoto model on cell complexes, `https://github.com/ibfzj/topological-kuramoto/` (2025).
[54] M. Zhang, G. S. Wiederhecker, S. Manipatruni, A. Barnard, P. McEuen, and M. Lipson, Synchronization of micromechanical oscillators using light, Physical Review Letters **109**, 233906 (2012).
[55] A. E. Motter, S. A. Myers, M. Anghel, and T. Nishikawa, Spontaneous synchrony in power-grid networks, Nature Physics **9**, 191 (2013).
[56] R. Olfati-Saber, J. A. Fax, and R. M. Murray, Consensus and cooperation in networked multi-agent systems, Proceedings of the IEEE **95**, 215 (2007).